Neuron, Vol. 32, 359–374, October 25, 2001, Copyright ©2001 by Cell Press

Human Ocular Dominance Columns as Revealed by High-Field Functional Magnetic Resonance Imaging

Kang Cheng,[1] R. Allen Waggoner, and Keiji Tanaka
Laboratory for Cognitive Brain Mapping
RIKEN Brain Science Institute and
CREST
Japan Science and Technology Corporation
2-1 Hirosawa
Wako, Saitama 351-0198
Japan

Summary

We mapped ocular dominance columns (ODCs) in normal human subjects using high-field (4 T) functional magnetic resonance imaging (fMRI) with a segmented echo planar imaging technique and an in-plane resolution of 0.47 × 0.47 mm^2. The differential responses to left or right eye stimulation could be reliably resolved in anatomically well-defined sections of V1. The orientation and width (~1 mm) of mapped ODC stripes conformed to those previously revealed in postmortem brains stained with cytochrome oxidase. In addition, we showed that mapped ODC patterns could be largely reproduced in different experiments conducted within the same experimental session or over different sessions. Our results demonstrate that high-field fMRI can be used for studying the functions of human brains at columnar spatial resolution.

Introduction

Among the many neuroimaging tools available for studying human brain functions, functional magnetic resonance imaging (fMRI) is the most widely used today. One advantage of fMRI over other imaging techniques is its relatively high spatial resolution. Exactly how high the spatial resolution can be depends on MRI hardware, pulse sequences, and imaging parameters, as well as brain architectures and functional modules to be studied. One fundamental feature of the cortical architecture is its columnar organization, that is, neurons with similar functional properties are clustered together to form repeated units across the horizontal extent of the cortex. The columns are an elemental cortical processing unit. It is therefore of extreme importance to elaborate the fMRI technique to study human brain functions involved in sensory processing and cognitive tasks at columnar resolution.

The system of ocular dominance columns (ODCs) is one of the clearest examples of the distinct functional architecture within the cortex. Neurons in the primary visual cortex (striate cortex or V1) are primarily driven by visual input from either the left or the right eye and are organized in periodic left-right stripes known as ODCs. ODCs were originally discovered in cats and macaque monkeys by using the single-cell recording technique (Hubel and Wiesel, 1962, 1968), and the spatial features of ODCs were subsequently demonstrated using a number of anatomical approaches (Hubel and Wiesel, 1972; Wiesel et al., 1974; Kennedy et al., 1976; Horton, 1984; Florence and Kaas, 1992) and optical imaging methods (Blasdel and Salama, 1986; Ts'o et al., 1990) in macaque monkeys. ODCs are composed of alternating slabs elongated along one axis on the surface. The strongest ocular dominance is observed in layer IVc (Hubel and Wiesel, 1968), where geniculocortical afferents serving the left and right eyes are strictly segregated. Cells are less purely monocular in the upper and lower layers (Hubel and Wiesel, 1968), but the dominance by one eye or the other is consistent throughout the entire cortical thickness (Kennedy et al., 1976; Tootell et al., 1988).

Although most of the methods used for studying monkeys cannot be applied to humans, the results from a few studies conducted on humans indicate that ODCs in humans are organized similarly to those in monkeys except that corresponding intercolumnar distances are larger in humans. Horton and colleagues (Horton and Hedley-Whyte, 1984; Horton et al., 1990) studied postmortem brains from patients who had undergone enucleation of one eye many years before death. By reconstructing ODCs of the two eyes differentially stained with cytochrome oxidase (CO), the authors demonstrated that human ODCs, just like ODCs in macaques, are oriented orthogonal to the V1/V2 borders (Figures 1A and 1B). In addition, human ODCs appear wider in the portion of V1 representing the central vision than in that representing the peripheral vision, and the widest ODCs are distributed near the V1/V2 borders. Although there is individual variation, human ODCs, measuring ~1 mm in width (see also Hitchcock and Hickey, 1980), are wider than those found in macaques, which measure ~0.4 mm in width. Human ODCs thus provide an ideal model for testing the spatial resolvability of fMRI (Menon et al., 1997; Menon and Goodyear, 1999; Dechent and Frahm, 2000).

The spatial resolution of fMRI measurements based on the blood oxygenation level-dependent (BOLD) technique (Ogawa et al., 1990; Turner et al., 1991; for review, see Ogawa et al., 1998) is ultimately limited by the interval between the vessels that primarily contribute to the signals. The distance between neighboring capillaries is a few tens of microns and that between vertically penetrating venules is around 0.5 mm (e.g., Duvernoy et al., 1981). However, before this ultimate limitation is approached, there are several possible limiting factors, including the signal-to-noise ratio (SNR). The SNR in an fMRI experiment is simplistically proportional to the voxel size. To map human ODCs, a small in-plane pixel size, for example, 0.5 mm on each side, is required. Thus, to retain a sufficient SNR with such small in-plane pixels, the slice cannot be made too thin. The SNR can be increased not only by increasing phase-encoding steps, narrowing sampling bandwidth, and increasing the total scan time, but also by using a high-field MRI system (Turner et al., 1993; Gati et al., 1997). Taken together, a reasonable SNR may be obtained at 4 Tesla

[1] Correspondence: kcheng@mailman.riken.go.jp

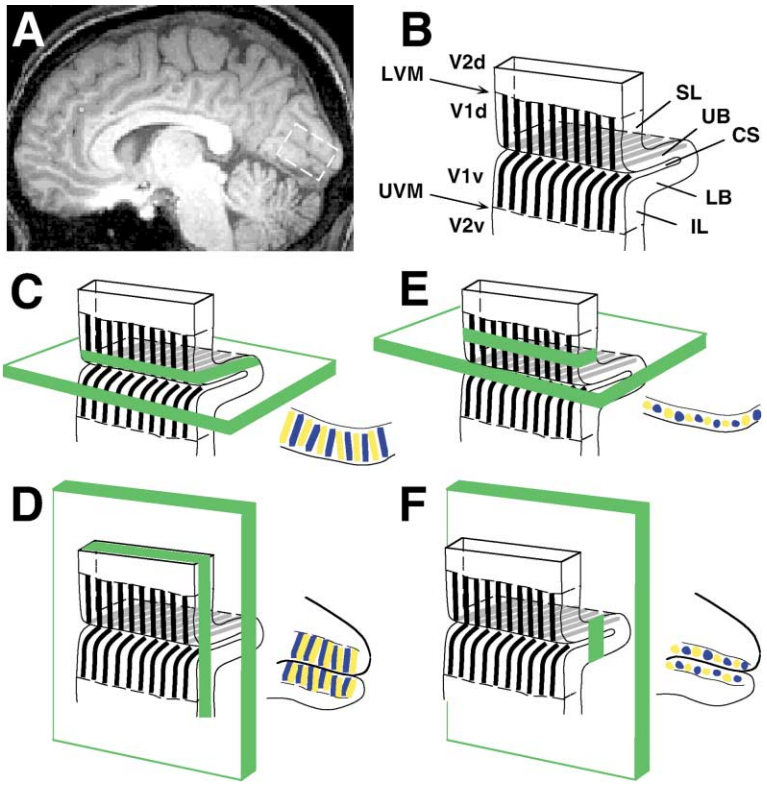

Figure 1. Orientation of Human ODC Stripes and Optimal Ways for Prescribing Slices

(A) An MR image shows the medial view of the right hemisphere. The medial occipital lobe around V1 (dashed rectangle) is schematically shown in (B).

(B) A cartoon diagram depicts the relationship between the orientation of human ODC stripes and the geometry of the calcarine V1 based on the observation by Horton et al. (1990). The opercular V1, which curves out toward the occipital pole, is not shown. ODC stripes run perpendicular to the V1/V2 borders (arrows) and the lips of the calcarine sulcus (CS). Abbreviations: UB and LB, upper and lower banks of the CS; SL and IL, superior and inferior lips of the CS; V1d and V1v, dorsal and ventral V1; V2d and V2v, dorsal and ventral V2; LVM and UVM, cortical representation of the lower and upper vertical meridians.

(C) An oblique slice is placed parallel to the CS to cover the UB (or equivalently the LB [not shown]). Mapped ODCs on such a slice will appear as alternating stripes, as schematically shown on the right (yellow and blue stripes represent left and right eye ODCs).

(D) A sagittal slice is placed to cover the medial surface (SL and/or IL). Mapped ODCs will appear as alternating stripes that terminate near the V1/V2 borders.

(E) An oblique slice, parallel to the CS or the V1/V2 border, is placed to cut the medial surface.

(F) A sagittal slice, parallel to the interhemispheric fissure, is placed to cut the UB and LB. Mapped ODCs on (E) and (F) will appear as alternating patches.

(T) for small voxels with an in-plane resolution of 0.5 mm and a slice thickness of 3–4 mm.

The spatial resolution of BOLD-based fMRI can also be limited by motions of the head and brain and by signals from large veins running on the surface of the brain. Special measures to minimize their influences should be provided. Moreover, there are geometric constraints imposed by the morphology of the functional architectures to be mapped. In order to map ODCs, it is essential to orient the slice properly so that the elongated voxels fall into individual columns rather than intersecting several columns, which will cause undesirable partial volume effects. How to realize this in individual subjects is a big experimental question for reliable mapping of ODCs using fMRI (Figures 1C–1F).

We had three straightforward goals in the present study. First, we wanted to measure to what extent the responses to prolonged monocular stimulation of the two eyes could be differentiated in anatomically well-defined sections of V1. Second, we wanted to see how voxels showing differential responses, if any, were clustered in these sections. Lastly, we wanted to test if the clustered patterns could be reproduced over different experiments.

Results

From all three subjects, ODC-like alternating stripes or patches were seen in anatomically well-defined sections of V1. These patterns were largely reproducible. The patterns from different subjects, however, showed large variation due to the difference in the shape of V1 among the subjects. For simplicity and completeness of presentation, the results below will be described based on illustrations mainly from a representative subject, with additional materials from the remaining two subjects. Quantitative analyses will be reported for all three subjects.

Slice Prescription Based on V1 Morphology

The anatomical details of a representative subject (subject 1) are given in Figure 2. The caudal part of the calcarine sulcus (CS) on the right hemisphere follows a straight course (Figures 2A and 2B), whereas the CS on the left hemisphere follows a curved course caudorostrally (Figure 2C). The three slices used in the main ODC experiment were optimally prescribed to cover the caudal part of dorsal V1 on the right hemisphere. On the right hemisphere, the posterior portion of the bottom slice (slice e-e′ indicated in Figures 2A–2D) included dorsal V1 up to 10° eccentricity (Figure 2E), which was ~3 cm from the occipital pole, similar to those reported previously (Horton and Hoyt, 1991; Sereno et al., 1995; Engel et al., 1997). As is evident in Figure 2E, the medial aspect of this section of V1 on the right hemisphere, particularly the cortex between ~3° and 10° eccentricities, had a relatively flat and wide appearance on the slice. This anatomically well-defined section of dorsal

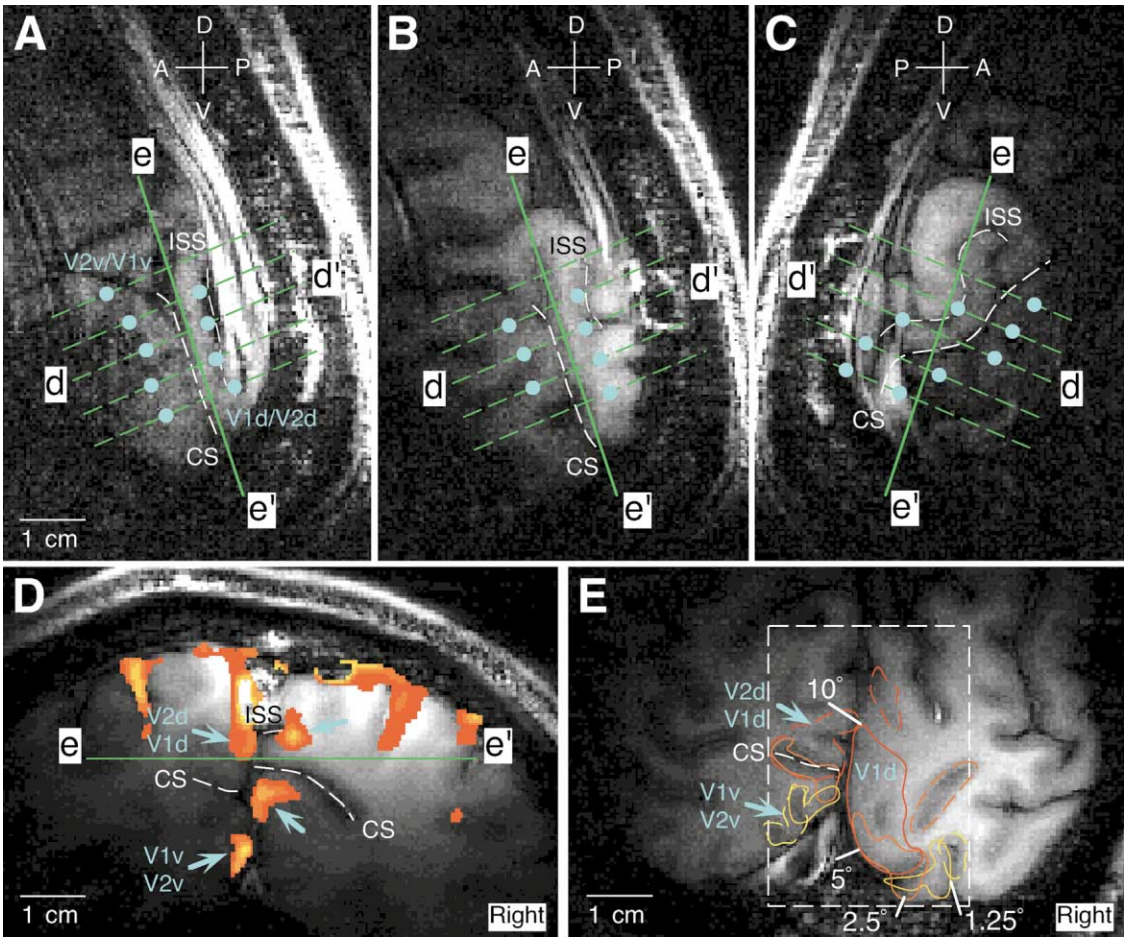

Figure 2. Anatomical Details of V1 of Subject 1

The shape of V1 is shown on the high-resolution sagittal scout images for the right (A and B) and left (C) hemispheres, respectively. (A) and (C) are the mesial slices, and (B) is 3 mm lateral to (A). The V1/V2 borders were mapped in five oblique slices perpendicular to the caudal CS on the right hemisphere. The results for the slice d–d′ (indicated in [A]–[C]) are shown in (D), where blue arrows indicate the mapped V1/V2 borders (see Figure 1B). Mapped V1/V2 borders on the five oblique slices were then projected onto the sagittal images (filled blue circles in [A]–[C]). The three slices used in the eccentricity mapping as well as the main ODC experiment were prescribed parallel to the caudal CS on the right hemisphere. The bottom slice that cuts through the upper bank of the caudal CS on the right hemisphere (see slice e–e′ in [A], [B], and [D]) is shown in (E). In (E), the composite eccentricity map (only for the cortex surrounding V1) is represented by the contours circumscribing regions activated by four rings of different sizes (radius: yellow, 0–1.25°; yellowish-brown, 1.25–2.5°; brown, 2.5–5°; red, 5–10°. Dashed contours indicate the sections of the gray matter that may not be confined to V1 completely). The V1/V2 borders on the left hemisphere in (E) (blue arrows) were determined in an extra experiment. Mapped ODCs from this subject are shown for the ROI indicated by the dashed rectangle in Figure 4. Abbreviations: A, anterior; P, posterior; D, dorsal; V, ventral; ISS, inferior sagittal sulcus. Other abbreviations are the same as those in Figure 1.

V1 was selected as our main region of interest (ROI) in this subject. The cortex representing dorsal V1 peripheral to the 10° eccentricity did not appear on this slice because the CS on the right hemisphere had a hooking appearance and its rostral part deviated away from the slice ventrally (Figure 2A). The relationship between the orientation of the bottom slice and the ODCs to be mapped on the right hemisphere was expected to follow the schema illustrated in Figure 1C. It should be stressed that this slice was not optimized for the left hemisphere because it cut through the CS on the left hemisphere at a large angle, as is evident in Figure 2C.

The second slice contained a part of the inferior sagittal sulcus (ISS) (Ono et al., 1990) on the right hemisphere, which ran parallel to the CS and was immediately above the dorsal V1/V2 border in this subject (Figures 2A and 2D). The third slice covered only a small part of the opercular V1 near the occipital pole and was out of the calcarine V1 anteriorly. ODCs were not expected to be optimally mapped on these two slices (data not shown).

Mapped ODC Patterns

Rigid head motion was suppressed by a physical fixation apparatus and the MRI signal fluctuation due to pulsatile and respiratory motions was minimized by a postprocessing procedure so that the in-plane mass-of-center fluctuation of time series images during the main ODC experiment was approximately twice that caused by the system noise estimated by imaging a phantom (Figures 3A–3D; see Experimental Procedures). The contribution

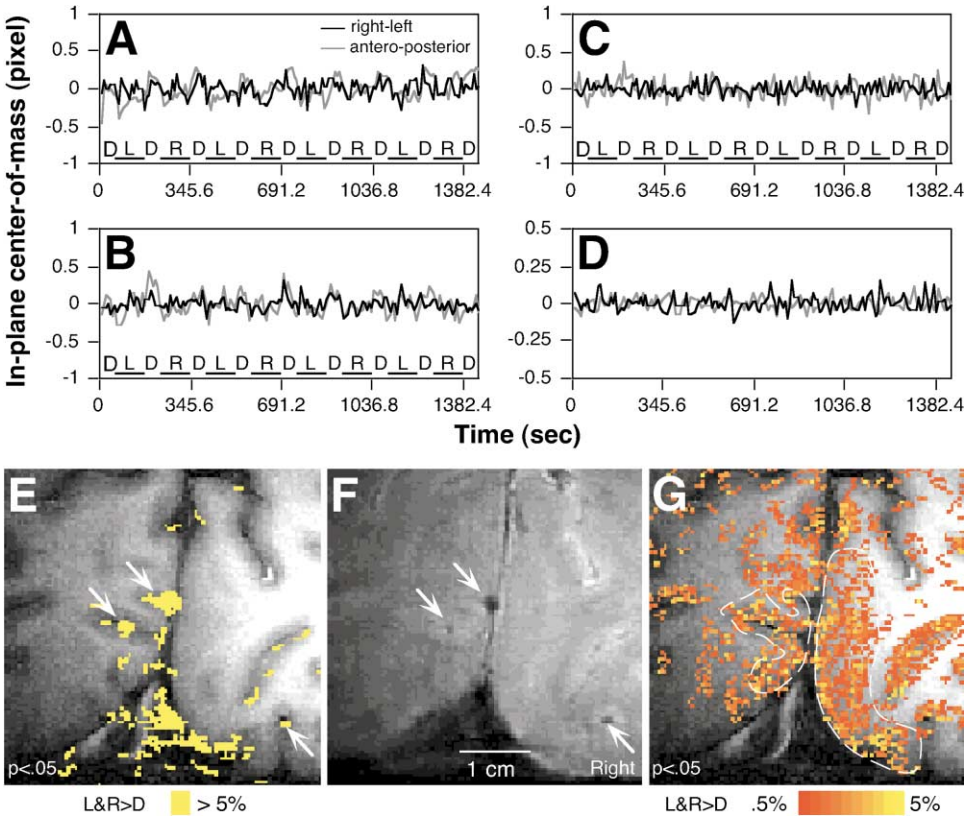

Figure 3. Corrections for Physiological Fluctuation, Rigid Head Motion, and System Drifts, and Removal of Voxels Associated with Large Veins

(A–D) The in-plane center-of-mass fluctuations of time series images acquired in an ODC experiment (subject 1) in right-left (black trace) and anteroposterior (gray trace) directions are shown *before* (A) and *after* (B) physiological fluctuation, rigid head motion, and system drifts were corrected. The ordinate represents the center-of-mass in each direction after the mean was subtracted away. The head motion in this experiment was restricted with a vise-like device, and mapped ODCs are shown in Figure 4. (C) shows the in-plane center-of-mass fluctuations obtained from another subject (subject 2, Figure 5) *after* corrections. The head motion in this experiment was restricted with a bite-bar system. For comparison, (D) shows the fluctuations of time series images acquired with identical imaging parameters on a phantom after system drifts were eliminated from raw data. Abbreviations: D, dark periods; L, left eye stimulation; R, right eye stimulation.

(E–G) How activated voxels associated with large veins were removed from an activation map is shown. The subject's anatomical details and mapped ODCs from the same experiment are shown in Figures 2 and 4, respectively. (E) Voxels with large signal changes (>5%) are mainly found in large draining veins or the sinus outside the brain tissue (gray matter) and appear darker in the corresponding EPI image due to their shorter T_2^* (F). Arrows in (E) and (F) indicate identical loci of identified vessels. (G) Voxels with signal changes smaller than 5% are distributed inside the gray matter. The dashed contours circumscribe V1 defined on this slice (see Experimental Procedures).

of large veins to the fMRI signals was minimized by removing activated voxels with signal change larger than 5% during left or right eye stimulation, compared with dark periods. The remaining activated voxels were well confined to the gray matter (Figures 3E–3G; see Experimental Procedures). We also paid attention when the slices were prescribed so that the pia of the cortex around the main ROI was avoided as much as possible. As a result, the main ROI was generally void of large veins running on the pial surface (see Figures 3E–3G, V1 on the right hemisphere).

The activation map obtained by comparing the images acquired during stimulation of one eye with those obtained during dark periods did not exhibit modular patterns. Figures 4A–4C show examples obtained at $p < 0.05$ using the slice similar to that shown in Figure 2E in subject 1. No alternating patterns resembling ODCs were observed in either activation map with left or right eye stimulation, and the patterns in the two maps were not complementary to each other (Figures 4A and 4B). Within the main ROI (indicated by the dashed contour on the right hemisphere in Figure 3G), the *total activated voxels* at this threshold, including those activated solely by stimulation of the left or right eye and those activated by stimulation of either eye compared with dark periods (Figure 4C), covered ~76% of the gray matter (~78% and ~74% in the other two subjects), and the overlapped voxels (voxels in red in Figure 4C) amounted to 68.3% of the total activated voxels, whereas those activated only by left or right eye stimulation (voxels in yellow and blue in Figure 4C) accounted for only 31.7%. The high percentage of overlapped voxels within the well-defined section of V1 was very consistent between repeated experiments on the same subject and was also very similar across the three subjects (68.8% ± 4.9%, mean ± SD). It should be pointed out that these observations were made independently of the threshold used. Even at much higher thresholds, the two activation maps

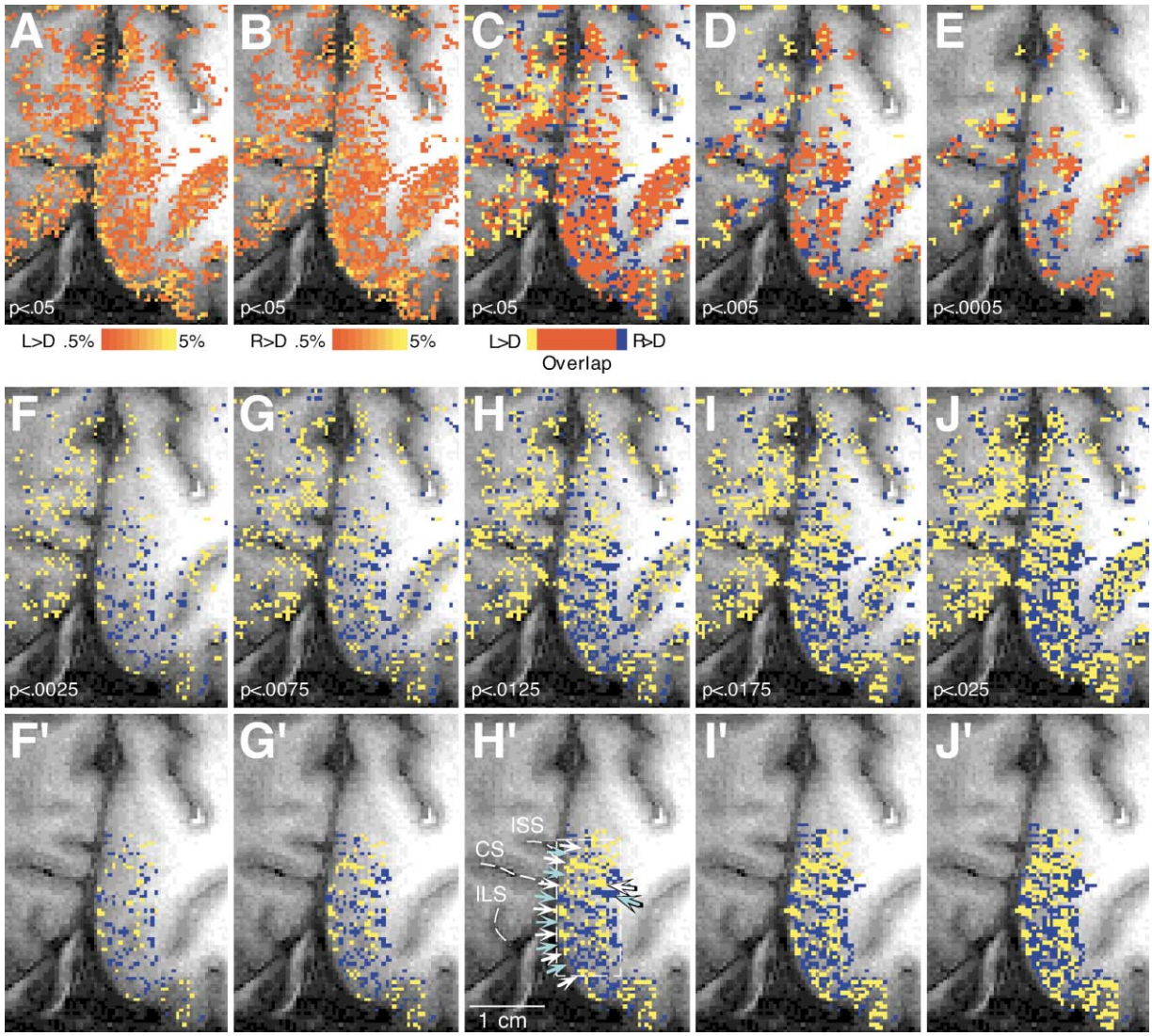

Figure 4. Activation Maps and ODC Maps Obtained from Subject 1

Activation maps show voxels activated by stimulation of the left (A) and right (B) eye, respectively, compared with dark periods ($p < 0.05$). The voxels associated with large veins have already been removed (see Figures 3E–3G). In (C), voxels in yellow and blue only satisfied the statistical criteria for activation by left or right eye stimulation, respectively, and those in red satisfied the criteria for activation by stimulation of either eye ($p < 0.05$). The maps similar to (C) at higher thresholds are shown in (D) ($p < 0.005$) and (E) ($p < 0.0005$). (F)–(J) illustrate ODC maps from the high ($p < 0.0025$) to low ($p < 0.025$) threshold. Voxels in yellow responded more to stimulation of the left eye than to that of the right eye, whereas those in blue responded more to stimulation of the right eye. Alternating ODC-like stripes are only seen in the anatomically well-defined section of V1 on the right hemisphere. For clarity, mapped ODCs at different thresholds are selectively shown in the dorsal V1 (V1d, see Figure 2E) of the right hemisphere (F′–J′). The dashed rectangle in (H′) shows the region in which the width of 15 mapped ODCs (indicated by white and light-blue arrows for left and right eye columns, respectively) was measured and test-retest patterns were compared (see Figure 9). Abbreviations: CS, calcarine sulcus; ILS, intralingual sulcus; ISS, inferior sagittal sulcus.

were still not complementary to each other, with overlapped voxels accounting for the majority of the total activated voxels (59.9%, $p < 0.005$, see Figure 4D; 55.6%, $p < 0.0005$, see Figure 4E).

Figures 4F–4J show ODC maps, which were generated by comparing images acquired during left and right eye stimulation, at five different thresholds (see Experimental Procedures). We did not attempt to justify a single significance level for thresholding the ODC map; rather, we showed maps at different thresholds because our purpose here was to see how voxels displaying ocular dominance at different levels were clustered over the entire activated area. Alternating ODC-like patches or stripes (referred to as mapped ODCs) were best observed within the main ROI, as shown separately in Figures 4F′–4J′ (in particular between 3° and 10° eccentricities, see description in the previous section). Outside the main ROI, the alternating pattern was not observed in the cortex immediately anterior, which was likely a part of dorsal V2. The only other part where we saw some alternating patches was a pocket of cortex lateral to the main ROI. This might include a portion of dorsal

V1; however, the slice was not optimally prescribed for mapping ODCs in this part of cortex. The most striking difference was probably in the left hemisphere, where the alternating pattern was conspicuously absent.

Several important points could be made by visually examining the mapped ODC patterns shown in Figures 4F′–4J′. First, the alternating stripes were oriented roughly orthogonal to the interhemispheric fissure. This was especially evident in maps at intermediate thresholds, such as the one shown in Figure 4H′. Second, a majority of stripes were already present in the map at the highest threshold (Figure 4F′), where 24% of the total activated voxels were assigned to either left or right ODCs and were merely broadened as the threshold was lowered (Figures 4G′–4J′, see also Figure 8G). Even in the map at the lowest threshold (Figure 4J′), where 96% of the total activated voxels (with potentially more random voxels) were assigned to either eye, the general appearance and number of alternating stripes did not change. This is consistent with the suggestion that the strength of ocular dominance across ODCs shifts gradually (e.g., Blasdel, 1992; Horton and Hocking, 1998, and see below). Finally, we measured peak-to-peak distances between neighboring columns along the narrow dimension (parallel to the interhemispheric fissure in this case) to estimate the width of mapped ODCs. The average width was 1.1 mm for 15 identified columns circumscribed by the dashed rectangle in Figure 4H′.

Similar results were obtained from the remaining two subjects (Figures 5 and 6). Figure 5 illustrates the anatomical details and mapped ODCs obtained from the second subject (subject 2). The slice was aligned to cover the lower bank of the CS on the left hemisphere because the lower bank was flatter than the upper bank in this subject (Figure 5A). As shown in Figure 5G, although alternating stripes or patches of mapped ODCs on the left hemisphere displayed a more complex pattern, it was evident that they, too, were oriented roughly perpendicular to the interhemispheric fissure, except for a small fraction near the occipital pole. The average width of mapped ODCs from this subject was 1.2 mm based on measurements of 18 columns on the left hemisphere. The average width from the third subject, measured from 16 columns in the upper bank of the CS on the left hemisphere, was 1.0 mm (Figure 6G). In addition, the results shown in Figures 5 and 6 also serve as good examples to demonstrate the importance of both the morphological quality of V1 to be mapped and the orientation of the slice to be selected in relation to the shape of V1. On the right hemisphere in both subjects, although the slice was roughly parallel to the CS and cut through the medial surface of ventral V1 (Figures 5B and 6B, see also Figure 1E), mapped ODCs (Figures 5F and 6F) appeared less regular and wider along the horizontal extent of the gray matter. As will be discussed below, this was most probably caused by the partial volume effect across multiple columns due to the fact that it was extremely difficult, if not impossible, to prescribe an oblique slice (see Figure 1E) that was strictly perpendicular to the stripes of ODCs to be mapped across the horizontal extent of cortex.

To quantify the observations described above, we performed two analyses on mapped ODCs from each subject. First, for each ODC voxel within the main ROI, we searched for the shortest distance (in unit of pixels) between the voxel and the remaining voxels preferring the same eye and that between the voxel and all the voxels preferring the opposite eye. For all ODC voxels, two distributions (percentage of voxels versus the shortest distance) were generated, one for the same eye preference (*same distribution*) and the other for the opposite eye preference (*opposite distribution*). The majority of voxels in the same distribution had the shortest distance of 1 (abutting each other), whereas many voxels in the opposite distribution had the shortest distance larger than 1 (segregated) (see Figures 7A–7E for subject 1). The two distributions at all five thresholds (for all three subjects) were significantly different ($p < 0.001$, Kolmogorov-Smirnov test). This result indicates that mapped ODC voxels preferring the same eye tended to cluster together.

In the second analysis, we Fourier-transformed the mapped ODC pattern at each threshold within the main ROI. The Fourier transform revealed a maximum in magnitude along the narrow dimension of mapped ODCs (i.e., parallel to the interhemispheric fissure for subjects 1 and 2, and parallel to the vertical terminal segment for subject 3), which appeared consistently at all five thresholds (e.g., see Figures 7F–7J for results from subject 1). Similar results were also obtained from the remaining two subjects. The maximum's repetition period was approximately twice the width of mapped ODCs that we estimated for each subject. Such a maximum of comparable magnitude was not seen in other directions. This result supports the existence of a repeated and oriented structure in the mapped ODCs.

In short, our observations on the orientation and width of mapped ODCs conform to those based on CO staining of postmortem brains (Horton and Hedley-Whyte, 1984; Horton et al., 1990).

Differential Responses to Monocular Stimulation

Differential responses in mapped ODCs were better appreciated in the time courses averaged for left and right eye dominant voxels, respectively, as demonstrated for subject 1 in Figures 8A–8D. In general, left or right eye dominant voxels showed consistently larger responses during all the four periods when the corresponding eye was stimulated (i.e., left eye stimulation periods for left eye dominant voxels and right eye stimulation periods for right eye dominant voxels) than those during the four periods when the opposite eye was stimulated. However, it is important to point out that voxels assigned to the left or right eye also responded substantially to the stimulation of the opposite eye. This was true whether the threshold was set high (Figures 8A and 8B) or low (Figures 8C and 8D). At the highest threshold ($p < 0.0025$), the average signal changes (quantitative analyses below were all performed on voxels within the main ROI, unless otherwise noted) when the corresponding eye and the opposite eye were stimulated were 1.99% and 0.82%, respectively, compared with the baseline, and at the lowest threshold ($p < 0.025$), they were 1.81% and 1.23%, respectively (Figure 8E). The responses observed when the opposite eye was stimulated may be due to the fact that cells are not completely monocular throughout the cortical thickness and the fact that voxels located on borders between neighboring columns cover both columns partially. These will be discussed in detail below.

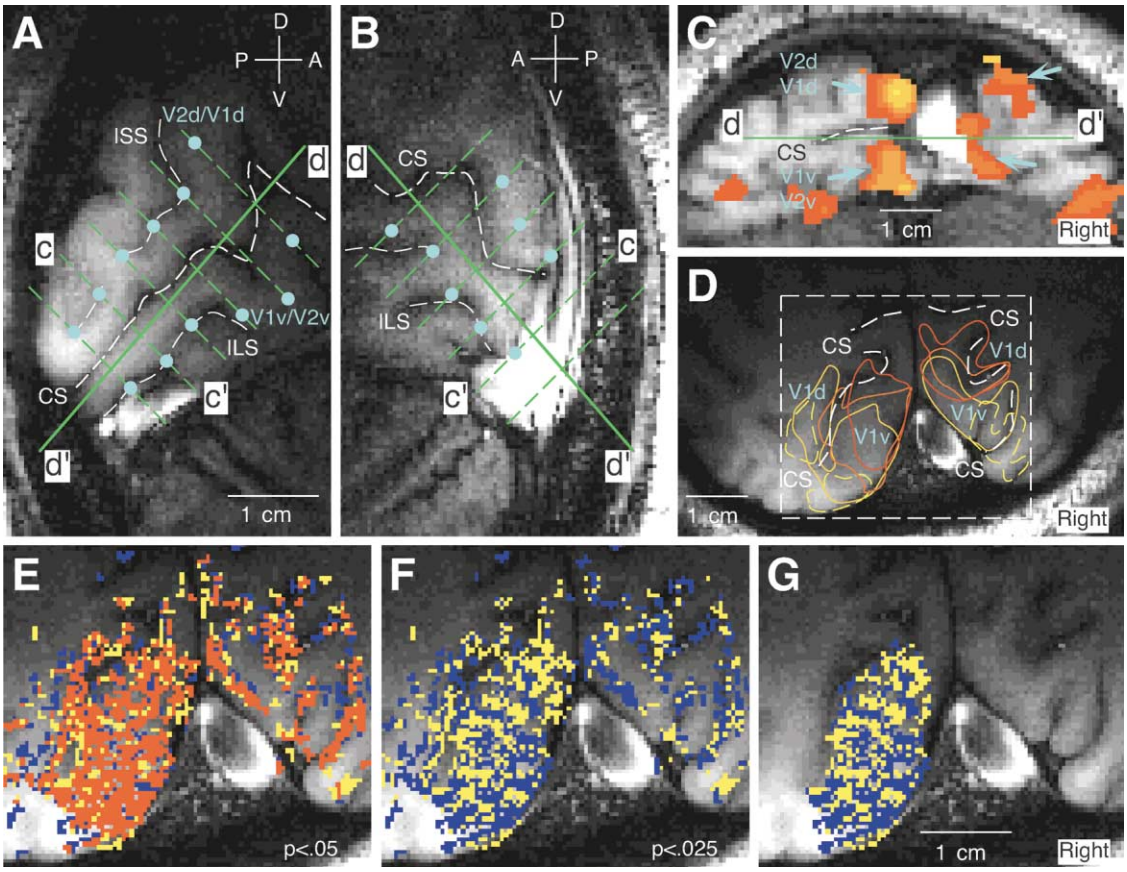

Figure 5. Anatomical Details of V1 and ODC Map Obtained from Subject 2

The shape of V1 is shown for the left (A) and right (B) hemispheres, respectively. The slices used in the remaining experiments were optimally prescribed for the lower bank of the CS on the left hemisphere. (C) shows the mapped V1/V2 borders (indicated by blue arrows) on slice c–c′ (indicated in [A] and [B]), and (D) shows the composite eccentricity map on the slice containing the main ROI (slice d–d′, indicated in [A]–[C]). In (E), voxels in yellow and blue were activated solely by stimulation of the left or right eye, respectively, and those in red were activated by stimulation of either eye ($p < 0.05$). (F) shows a low threshold ($p < 0.025$) ODC map. For clarity, mapped ODCs are selectively shown in the ventral V1 (V1v, see [D]) of the left hemisphere (G). Other abbreviations and conventions are the same as those in Figures 2 and 4.

To quantify the differential response, we calculated the ratio of the average signal change in mapped ODCs when the corresponding eye was stimulated to the average signal change when the opposite eye was stimulated (i.e., the ratio between the lengths of two paired bars shown in Figure 8E). This ratio was termed the differential response ratio (DRR). For subject 1, the DRR was 2.34 at the highest threshold and 1.47 at the lowest threshold (Figure 8F). Among the three subjects, the DRRs were very similar at each threshold: 2.24 ± 0.12 (mean ± SD) at the highest threshold and 1.45 ± 0.04 at the lowest threshold (Figure 8F). We have mentioned in the previous section that as the threshold decreased, mapped ODCs were merely broadened. Figures 8F and 8G show that the gradual broadening of mapped ODCs was correlated with the gradual decrease of the DRR, thereby supporting quantitatively a gradual shift in the strength of ocular dominance across ODCs.

Test-Retest Patterns of Mapped ODCs

The exact appearance of mapped ODCs depends on the V1 morphology among other factors, and currently there is no other way to verify mapped ODCs in humans. In addition, time courses averaged from selected voxels, such as those shown in Figures 8A–8D, depend on how the voxels are chosen and do not carry information about the spatial feature of mapped ODCs. Therefore, it is important to reproduce mapped ODC patterns no matter what they look like. The reproducibility in our study was first investigated by comparing mapped ODC patterns acquired in two successive experiments within a single experimental session as well as those obtained from a single subject in different sessions.

Figures 9A–9C show the results of comparing the two ODC maps obtained from subject 1 within the same session. The map shown in Figure 9A was identical to that shown in Figure 4J′, and the map in Figure 9B was obtained in the second experiment. The respective territories occupied by the left and right eye columns were largely preserved, although some columns appeared to have different widths between the two maps. Figure 9C shows overlapped voxels in the two maps that were assigned to the same eye. These voxels in Figure 9C constituted 63.3% and 62.7% of the total assigned voxels in Figures 9A and 9B, respectively. The average of the two ratios, named the overlap ratio (OR), is 0.63. The essential feature of ODCs in this section of V1 is clearly captured by the overlapped ODC map, which to

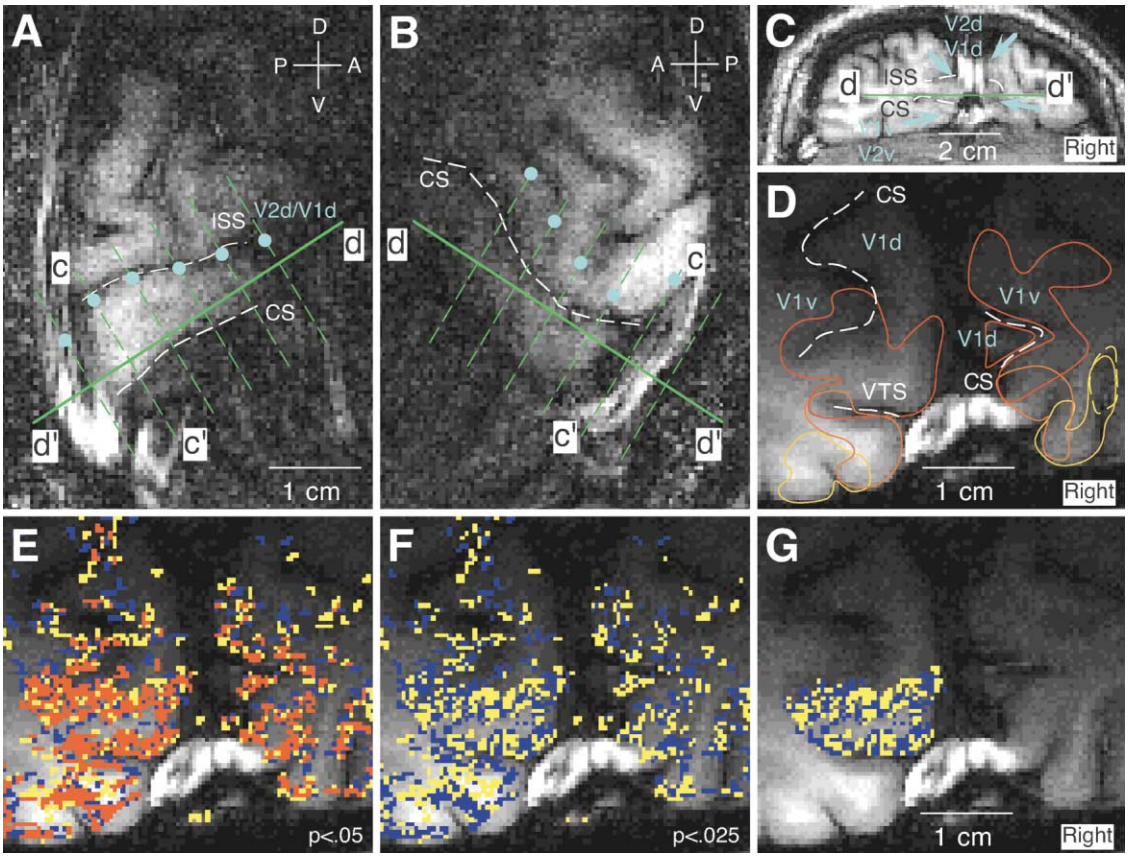

Figure 6. Anatomical Details of V1 and ODC Map Obtained from Subject 3

The shape of V1 is shown for the left (A) and right (B) hemispheres, respectively. The slices used in the remaining experiments were optimally prescribed for the upper bank of the CS on the left hemisphere. (C) shows the mapped V1/V2 borders (indicated by blue arrows) on slice c–c′ (indicated in [A] and [B]), and (D) shows the composite eccentricity map on the slice containing the main ROI (slice d–d′, indicated in [A]–[C]). VTS, vertical terminal segment (also referred to as the extreme calcarine sulcus; see Ono et al. [1990]). Other abbreviations are the same as those in Figure 2. Conventions in (E)–(G) are identical to those in Figures 5E–5G except that mapped ODCs in (G) are shown in the dorsal V1. Note that the narrow dimension of mapped ODCs in this subject is parallel to the VTS. The discontinuous activation in the center of the main ROI was due to the fact that the upper bank of the CS in this subject is slightly bent.

a large extent resembles mapped ODCs at intermediate thresholds (compare Figure 9C with Figures 4G′ and 4H′). A similar OR (0.59) was also obtained in the two within-session experiments conducted on subject 2.

Figures 9D–9F show the results of comparing the two ODC maps acquired from subject 1 in two sessions. The ODC map in the first session (Figure 9D) was the same as the one shown in Figure 9A, and the ODC map in the second session (Figure 9E) was obtained approximately 3 months later. We exerted special effort in the second session to position the slice as close as possible to that in the first session. The anatomical match between the two ODC maps was achieved manually with the help of the three prominent sulci on the left hemisphere—that is, the ISS, the CS, and the intralingual sulcus (ILS) (Figure 4H′). As shown in Figures 9D and 9E, the overall patterns of mapped ODCs in the two sessions resemble each other in appearance, although they are less overlapped (Figure 9F, the OR is 0.48). The lower OR compared to the within-session comparison was most probably due to the imperfect match of slice positions between the two sessions.

The reproducibility of mapped ODCs was further quantified as follows. For each ODC map, a value 1, −1, or 0 was first assigned to voxels preferring the left eye (in yellow color), the right eye (in blue color), or neither eye (blank voxels), respectively, and the mapped ODC pattern was smoothed with a Gaussian filter (FWHM = 2 in-plane pixels) (e.g., Figures 9G–9I [their corresponding unsmoothed maps are shown in Figures 9A, 9B, and 9E]). We then calculated the correlation coefficient of the values (ranging from 1.0 for the left eye to −1.0 for the right eye) between the corresponding voxels in the two smoothed maps to be compared. A high correlation was found between the two maps acquired within the same session ($r = 0.627$ [$p < 0.001$] for subject 1, see Figure 9J; $r = 0.485$ [$p < 0.001$] for subject 2). A lower but still significant correlation was also found between the two maps acquired in different sessions ($r = 0.372$ [$p < 0.001$] for subject 1, see Figure 9K).

These results demonstrate that mapped ODCs are largely reproducible over different experiments.

Discussion

In the present study, we have demonstrated that high-field fMRI can be used for mapping cortical columns such as ODCs in human V1. A unique feature in our

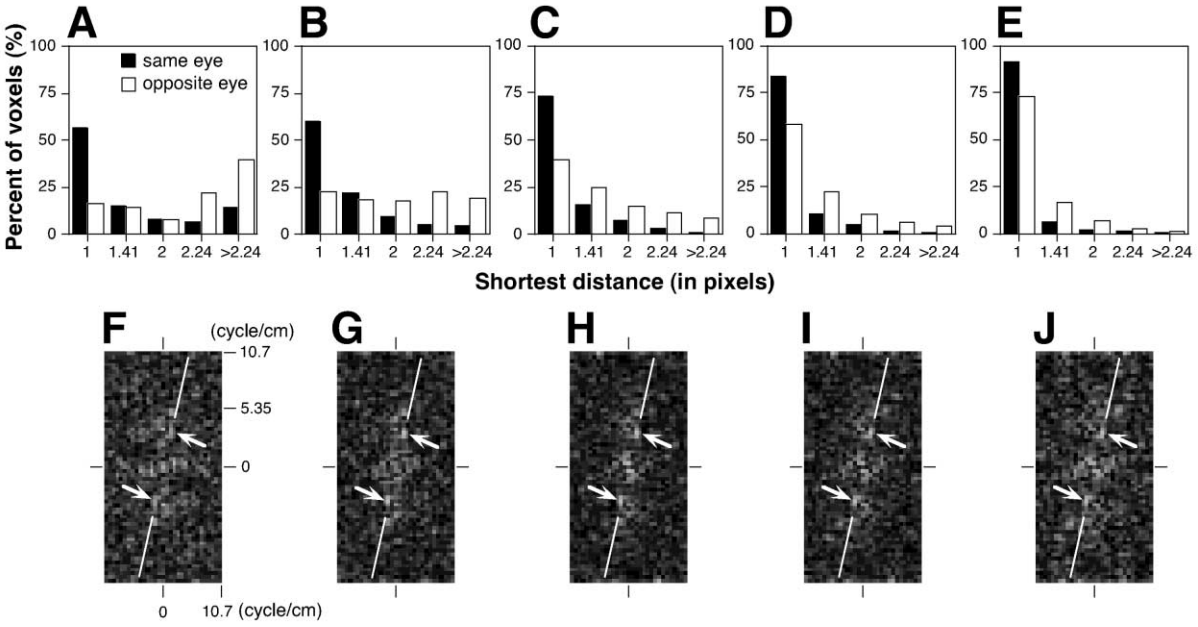

Figure 7. Distributions of Shortest Distances between Voxels Preferring the Same Eye and Opposite Eye, and Two-Dimensional Fourier Transforms of Mapped ODC Patterns

(A)–(E) show the distributions of the shortest distance between voxels preferring the same eye (filled bars) and between voxels preferring the opposite eye (open bars) at five thresholds for subject 1. The corresponding ODC maps are shown in Figures 4F′–4J′. The pair of distributions at each threshold was significantly different ($p < 0.001$, Kolmogorov-Smirnov test). (F)–(J) show Fourier transforms of mapped ODC patterns at five thresholds (see Figures 4F′–4J′). The white line segments in each figure indicate the direction of the maximum (indicated by the arrows), which in this subject is parallel to the interhemispheric fissure.

study was that the selected subjects all had a section of V1 that was flat, less sulcated and retinotopically well defined, and the slice used in the main ODC experiment was optimally prescribed in this well-defined section to preserve the genuine spatial relationship of ODCs to be mapped. The fact that the alternating pattern (mapped ODCs) appeared only in the anatomically well-defined section of V1 in each subject and it could be largely reproduced over different experimental sessions strongly indicated that the mapped ODCs reflected an underlying functional architecture (i.e., real ODCs) but not random noises. In the following sections, we will discuss these findings in relation to several important issues.

BOLD Responses and Spatial Resolvability

From the basic theory of the BOLD effect, the imbalance in the changes of cerebral blood flow (CBF) and cerebral metabolic rate of oxygen ($CMRO_2$) during activation, which alters the local content of deoxygenated hemoglobin (Hb), is thought to be the primary physiological phenomenon that causes the BOLD signal change. During activation, CBF increases much more than $CMRO_2$, and consequently, the venous blood is more oxygenated and the decrease in Hb leads to the increase in the BOLD signal.

Several BOLD-based fMRI studies in humans have reported an early BOLD signal decrease that appears for 2–3 s after the stimulus onset ("initial dip," Ernst and Hennig, 1994; Menon et al., 1995; Hu et al., 1997; Yacoub and Hu, 1999). The initial dip was interpreted as evidence for an early increase in Hb prior to the onset of a much larger CBF increase, similar to that observed by optical imaging in nonhuman mammals (e.g., Malonek and Grinvald, 1996; Malonek et al., 1997). Using an optical imaging spectroscopic approach, Malonek and Grinvald (1996) have shown that the early increase in Hb is more localized to individual orientation columns than the subsequent blood volume increase.

These findings have increased our hopes for using fMRI with the initial dip to map functional architectures. However, a number of controversies still remain regarding the existence of the initial dip in fMRI measurements (e.g., Fransson et al., 1998) and even the early increase in Hb (e.g., Jones et al., 2001; Lindauer et al., 2001). To date, except for a single study that mapped orientation columns in anesthetized cats (Kim et al., 2000), other attempts to use this component to map cortical columns in humans have not been successful even at high fields (4 T or higher). Other than the above-mentioned controversies, the primary reason for the failure may be the brief nature of the initial dip. The initial dip lasts very briefly (2–3 s) and then changes polarity to the late positive signal. The time required for acquiring even a single image at a spatial resolution sufficient for mapping cortical columns in humans is typically 4 s or longer. Moreover, multiple images over a prolonged stimulation period are usually needed to improve the SNR. Therefore, it is extremely difficult to use the initial dip in human studies at high spatial resolution.

Thus, the issue is whether the change of the later, much larger and sustained positive BOLD signal during prolonged stimulation is spatially localized or widely diffused. Recently, by measuring the increases of CBF and BOLD signal simultaneously under prolonged visual stimulation and a hypercapnia baseline condition, sev-

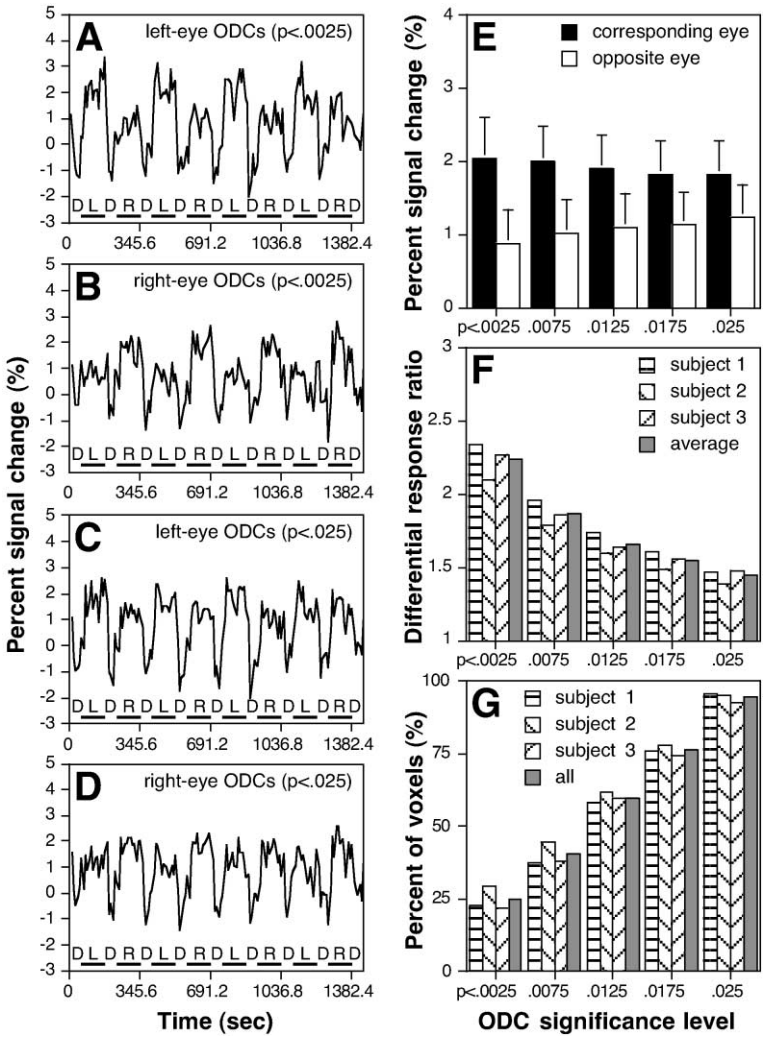

Figure 8. Time Courses and Differential Responses to Sustained Monocular Stimulation

Average time courses are shown in (A) and (B), respectively, for left and right eye dominant voxels within the main ROI in a high-threshold ODC map ($p < 0.0025$, Figure 4F′) obtained from subject 1. Time courses in a low-threshold map ($p < 0.025$, Figure 4J′) are shown in (C) and (D). Periods of stimulation of the left (L) or right (R) eye, separated by dark periods (D), are indicated by line segments below each time course. (E) shows the average signal changes of identified voxels during periods of stimulation of the corresponding eye (filled bars) and during periods of stimulation of the opposite eye (open bars) at five different thresholds (see Figures 4F′–4J′). The two values for each threshold were the means of average signal changes from both left and right eye dominant voxels for corresponding and opposite eye stimulation, respectively, and the error bars are the standard deviations. (F) shows the differential response ratios, defined as the ratio of the average signal change during stimulation of the corresponding eye to that during stimulation of the opposite eye at a given threshold, for each subject and the averages between subjects ($n = 3$). In (G), percentages of total activated voxels that could be differentially identified at five different thresholds are given for each subject and for all the subjects ($n = 3$). Data shown in (E)–(G) were calculated using voxels within the main ROI defined for each subject.

eral groups have demonstrated that there is a contribution of $CMRO_2$ increase to BOLD responses throughout the prolonged visual stimulation (Davis et al., 1998; Hoge et al., 1999; Kim et al., 1999; Schwarzbauer and Heinke, 1999). The $CMRO_2$ increase partially cancels out the positive BOLD signal caused by the CBF increase.

There is no consensus on the spatial specificity of CBF regulation. According to one model, the $CMRO_2$ increase during activation at a site comparable to the width of cortical columns occurs on a fine spatial scale, whereas CBF is controlled on a much coarser scale (Malonek and Grinvald, 1996). According to another model, the increases in both CBF and $CMRO_2$ during activation may take place on a fine spatial scale, and a larger CBF increase is needed to support a smaller $CMRO_2$ increase through the imperfect vessel-tissue diffusion (Buxton and Frank, 1997). Both models can be used to explain the BOLD behavior at low spatial resolution. At high spatial resolution, and at columnar resolution in particular, the two models would predict the relative magnitudes of the BOLD signal in activated and inactivated columns very differently. The fine spatial control of CBF would result in a larger BOLD signal in activated columns than in inactivated columns, whereas the coarse spatial control of CBF would lead to the opposite conclusion, that is, a smaller BOLD signal in activated columns. At any rate, as far as mapping ODCs is concerned, as long as the $CMRO_2$ increase occurs within individual columns under stimulation, the spatial specificity should be reflected by sustained positive BOLD signal, whether the CBF regulation is widespread or spatially confined.

In fact, even with short (2–4 s) visual stimulation, the data of the optical spectroscopic work by Malonek and Grinvald (1996) show that the differential Hb signal between activated and inactivated orientation columns persisted throughout the entire time course of responses. This was true even after Hb changed its polarity from increase to decrease, though the differential signal was bigger in the initial 2–8 s after the stimulus onset than that in the later period. Because a prolonged stimulation continues to activate neurons in activated columns, which leads to sustained $CMRO_2$ increase there, we expect a bigger differential signal between activated and inactivated columns when prolonged stimulation is used than that in the later period after a short stimulation is turned off.

The idea to utilize the differential signal due to differ-

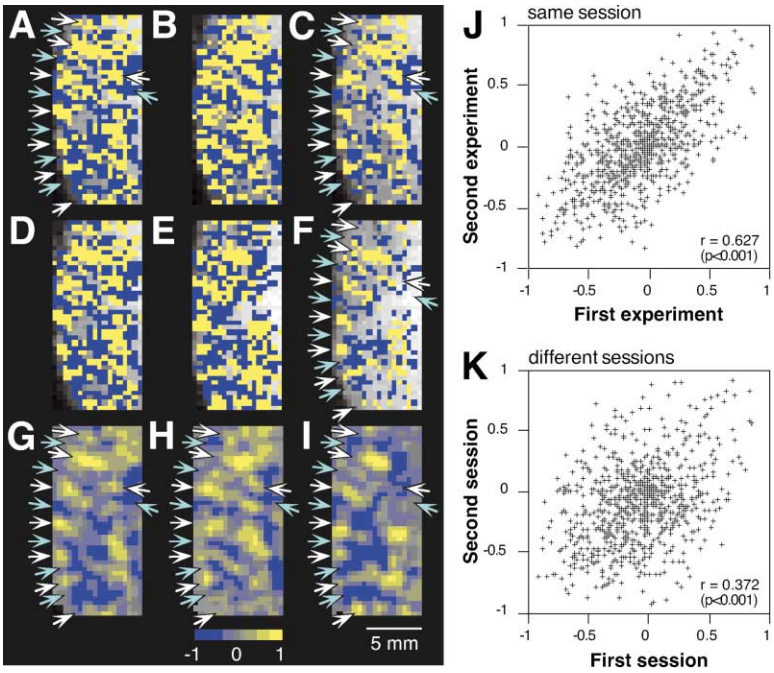

Figure 9. Reproducibility of Mapped ODC Patterns

(A) is identical to the map shown in Figure 4J′, and the ROI in which mapped ODCs are shown in this figure is shown in Figure 4H′ (dashed rectangle). Voxels in yellow responded more to stimulation of the left eye than to that of the right eye, whereas those in blue responded more to stimulation of the right eye. (B) is an ODC map ($p < 0.025$) obtained from the same ROI of the same subject in another experiment conducted within the same experimental session as in (A). Overlapped voxels assigned to the same eye in (A) and (B) are shown in (C). The voxels that overlapped but were assigned to the opposite eye are not shown. (D) and (E) are ODC maps obtained from the same subject in two sessions separated by approximately 3 months. Overlapped voxels assigned to the same eye in (D) and (E) are shown in (F). (G)–(I) illustrate smoothed patterns of ODC maps shown in (A), (B), and (E), respectively (see text). Arrows in (A), (C), and (G)–(I) which are identical to those shown in Figure 4H′, are shown to facilitate readers' observation. (J) and (K) are the scatter plots of the values of voxels shown in (H) and (I), respectively, against the values of corresponding voxels shown in (G).

ential $CMRO_2$ changes in the positive BOLD signal was adopted by Menon and Goodyear (1999). But, they used a short (4 s) visual stimulation and took images during a short period during and immediately after the stimulation. For the same reason described above for imaging with the initial dip, this method does not fully get the benefit of obtaining higher SNR by averaging images over time.

One potential problem of using sustained positive BOLD signal, however, is the artifacts from large veins. By optical imaging, Grinvald and colleagues have demonstrated that identical monkey ODC maps can be generated using either the early or late optical components, the only difference being that the vessel artifacts in the late-component map cannot be removed completely even with the differential mapping method (Grinvald et al., 2000, see their Figure 2). With 4 T fMRI and appropriate postprocessing, this problem can be avoided or minimized (see Experimental Procedures).

In our ODC experiment, each period of monocular stimulation lasted 115.2 s with a temporal resolution of 9.6 s. Since the first image in each period was excluded from statistical analysis to account for the hemodynamic delay, the BOLD signal used for differentiating left and right ODCs was exclusively obtained from the sustained positive phase (Figures 8A–8D). The ODC experiment in all three subjects was targeted on morphologically equivalent sections of V1 in relation to the orientation of the slice. Consequently, mapped ODCs obtained from the three subjects were found to be very similar in terms of spatial arrangement (orientation and average width) and magnitude of differential responses. These results demonstrate clearly that under optimal imaging conditions, the sustained positive BOLD signal can be used for spatially resolving functional architectures such as ODCs. However, as discussed in the previous paragraph, we cannot address the question whether the correlation between the differential components of BOLD signal changes and neuronal activity is positive or negative. It is possible that cells in voxels with larger BOLD signal changes during one eye stimulation (compared with the other eye stimulation) were actually less activated by the stimulation of the eye. Such a question may be answered by conducting similar experiments on cats or monkeys in combination with single-cell recordings.

Responses to Opposite Eye Stimulation

In our study, substantial responses were observed in the time courses when the opposite eye was stimulated. The DRR averaged from the three subjects ranged from 2.24 (translated into an inverse ratio of 0.45, or a 45% response when the opposite eye was stimulated compared to that when the corresponding eye was stimulated) at the highest threshold to 1.45 (69%) at the lowest threshold. Similar observations were made by Menon and Goodyear (1999), who reported a similarly defined ratio of 1.74 (57%) at a threshold presumably in between the two extreme thresholds used in our study.

The responses to the opposite eye stimulation may be partly due to the spreading of the BOLD signal across columns, especially the spreading of the CBF component. They are also partly due to the nature of ODCs: there are several lines of evidence that ODCs are not purely monocular by nature. Studies in monkeys have shown that, although the strongest ocular dominance is observed in layer IVc, cells in the upper and lower layers are less monocular (Hubel and Wiesel, 1968). Anatomically, intrinsic connections within V1 provide rich sources for binocular interactions (for review, see Cal-

laway, 1998). The long-range lateral connections in layers II and III are not completely restricted to the same-eye columns (Malach et al., 1993; Yoshioka et al., 1996). The massive feedback projection from layer VI pyramidal neurons to layer IV is usually not confined to the home columns (Wiser and Callaway, 1997). It has also been proposed that across ODCs, the ocular dominance gradually swings back and forth and largely binocular border strips exist in between largely monocular core zones (e.g., Blasdel, 1992; Horton and Hocking, 1998). In our ODC experiment, since the long dimension of voxels (i.e., the 3 mm slice thickness) ran through the cortical layers ($\sim$2.5 mm thick, e.g., Leuba and Kraftsik, 1994) in the main ROI, both the gradual shift of ocular dominance strength across mapped ODCs and the somewhat binocular responses even in the most monocular single voxels were expected. The averaging within the in-plane size of voxels (0.47×0.47 mm^2) should have further smoothed the strength of ocular dominance. Our results agree with these expectations.

It should be emphasized that the above-mentioned factors that cause substantial BOLD signal changes when the opposite eye is stimulated are intrinsic to the local neuronal activity and imaging parameter settings (e.g., in-plane resolution). In other words, this means that this portion of signal changes should be present throughout the stimulation regardless of whether the initial dip (if it is observable) or the later positive BOLD signal is used. Their presence makes it difficult to create a functional map by a direct mapping method (i.e., comparing left or right eye stimulation with dark periods) as has been shown in our results (Figures 4A–4E) and those in Menon and Goodyear (1999; but see Dechent and Frahm, 2000, in which very little response was observed when the opposite eye was stimulated). On the other hand, the differential mapping method appears to be a much better choice for revealing cortical architectures that are complementary in nature, such as ODCs and orientation columns, and should be used whenever applicable. The advantage of the differential mapping method over the direct mapping method has been extensively discussed in optical imaging literature (e.g., Blasdel, 1992; Grinvald et al., 2000) and is fully supported by our results.

Geometry of V1 and Slice Prescription

The imaging voxels used in our experiment were relatively small ($0.47 \times 0.47 \times 3$ mm^3). This size was determined so that the voxels were sufficiently small to reveal individual ODCs and at the same time sufficiently large to retain a sufficient SNR. In order to map ODCs with such elongated voxels, we carefully selected subjects who had a flat and less sulcated section of V1 (the main ROI) and optimally prescribed the slice so that the voxels would fall into individual columns rather than obliquely intersecting several columns. As demonstrated for the three subjects in the present study, an oblique slice containing the (flat) upper or lower bank of the (partially straight) CS appeared to be ideal (Figure 1C). With such a slice, we found that the average width and differential responses measured from mapped ODCs across all three subjects were very similar, and the orientation and average width of mapped ODCs were also in agreement with those reported previously (Horton and Hedley-Whyte, 1984; Horton et al., 1990).

Presumably, a sagittal slice can also be prescribed to cover ODCs in V1 that is exposed on the medial surface (Figure 1D). The sagittal slice will allow us to observe alternating stripes with differential responses similar to those revealed by the oblique slice containing ODCs in the upper or lower bank of the CS. Furthermore, mapped ODCs on the sagittal slice can be additionally validated because they should end abruptly near the V1/V2 borders. However, using such a sagittal slice will require that the subject's V1 on the medial surface is flat both anteroposteriorly and dorsoventrally. We have not found a single subject, including those screened for other experiments, whose V1 morphology satisfies this requirement.

An alternative is to prescribe an oblique slice that is parallel to the CS but cuts through the medial surface (superior or inferior to the CS, Figure 1E) or (similarly) a sagittal slice that cuts through the upper and lower banks of the CS (Figure 1F). Mapped ODCs on such slices in general appear as alternating patches (e.g., see Menon and Goodyear, 1999), but their exact appearance depends on the intersection angle between the slice and the axis of stripes of ODCs. Because ODC stripes are usually oriented irregularly locally although they tend to show a dominant orientation (e.g., see cases shown in Figures 15 and 16 in Horton and Hedley-Whyte, 1984), it is almost impossible to align a slice orthogonal (within $\pm$ 15°) to the stripes of ODCs. When the slice intersects real ODC stripes at an acute angle, a single elongated voxel will fall into more than one column obliquely, thereby causing a special type of partial volume effect. Our simulation results reveal that both the apparent width and the differential response of mapped ODCs are sensitive to the intersection angle. In these simulations, it is assumed, for the simplicity, that ODCs are purely monocular throughout the cortical thickness and 1 mm in width without binocular transition. When the intersection angle is within $90° \pm 15°$, mapped ODCs are approximately the same as real ODCs in terms of both width and differential response. When the intersection angle is smaller than 75°, the mapped ODCs start to widen gradually ($\sim$2 mm at 30°), and the maximum differential response drops rapidly. Mapped ODCs in some of our experiments, such as those shown in Figures 5F and 6F (both in the right hemisphere), therefore, can be explained by these simulation results. The mapped patterns in these cases do not reflect the real nature of ODCs.

Conclusion

In conclusion, fMRI at 4 T or higher fields (e.g., Yacoub et al., 2001) is suitable for mapping cortical architectures in humans as long as the architectures are complementary in nature, as are ODCs. One of the major difficulties in mapping human ODCs appears to stem from the geometric constraints imposed by the morphology of V1 in which they are embedded. While ODC-like alternating patterns can be revealed by taking careful experimental and analytical measures, the interpretation and quantification of mapped patterns need to be made with caution.

Experimental Procedures

General Procedures

Three subjects (male, ages 26–36) with no past history of psychiatric or neurological diseases participated in multiple sessions of the experiment, which were approved by the RIKEN Functional MRI Safety and Ethics Committee. The subjects were selected after the initial morphological screening of high-resolution three-dimensional anatomical MR images ($1 \times 1 \times 1$ mm^3) from a larger subject pool recruited within the RIKEN Brain Science Institute for the present and other fMRI experiments. In these selected subjects, the calcarine sulcus (CS) follows a straight course and the cortex around V1 is flat and less sulcated in at least one hemisphere (referred to as "good hemisphere"). All subjects had corrected-to-normal vision (see below) and gave their written informed consent.

Imaging Hardware and Visual Stimulation

All experiments were conducted on a Varian Unity Inova 4 T whole-body MRI system (Varian NMR Instruments, Palo Alto, CA) equipped with a Magnex head gradient system (up to 3.4 gauss/cm with a rise time of ~160 μs, Magnex Scientific Ltd., Abingdon, UK). High-resolution three-dimensional T_1-weighted anatomical MR images were scanned with a bird-cage radio-frequency (RF) coil (The John P. Robarts Research Institute, London, Ontario) or a transverse electromagnetic (TEM) RF coil (HF Imaging & Bioengineering, Inc., Minneapolis, MN). A 3 inch transmit/receive RF surface coil was used to acquire functional and anatomical images in the main ODC experiment. The surface coil was mounted on a bakelite support frame attached to the patient table. This coil allowed us to observe the posterior portion of the occipital lobe with higher SNR. During the experiment, the subject was made to lie supine on the patient table and to rest the back of his head on the surface coil or the bottom part of the bird-cage or TEM coil. Rigid head motion was restricted with a vise-like device padded with spongy rubber or a bite-bar system. It turned out that both methods worked equally well for our subjects as assessed by the in-plane center-of-mass fluctuation of time series images (see Figures 3A–3C and below). We nevertheless used several (two to four) pressure sensors placed around the subject's head to monitor any head motion during the experiment. This was to make sure that the position of the subject's head did not deviate from a reference position from the beginning to the end. The subject's heartbeat was monitored with a pulse oximeter, and respiration was monitored with a pressure sensor placed on the umbilical region. Both signals were recorded along with the timing of RF pulses for later corrections of physiological fluctuations.

Visual stimuli generated on two Macintosh computers were delivered to the subject's eyes via a pair of independently controlled optic fiber bundles (Silent Vision binocular glasses, Avotec Inc., Jensen Beach, FL) subtending 30° horizontally and 23° vertically. Corrected-to-normal vision for individual subjects was achieved by adjusting two refractive correction pieces built on the binocular glasses. The luminosity of the homogenous white color measured on the binocular glasses was ~4 Lux and that of the homogenous black color was ~0.5 Lux (measured with Extech 403125 Light ProbeMeter, Extech Instruments Co., Waltham, MA), resulting in a contrast of 8.

V1/V2 Borders, Eccentricity, and Slice Prescription

At the beginning of each experiment, a horizontal scout image running through the CS was obtained. Seven high-resolution (0.47×0.47 mm^2; slice thickness = 3 mm) sagittal anatomical images parallel to the interhemispheric fissure were then prescribed on the scout image and scanned with an inversion recovery FLASH pulse sequence (eight segments; TR = 19 ms; TE = 10 ms; TI = 1.3 s; delay time between segments = 2 s; number of averaging = 4). The CS on both hemispheres could be clearly identified on these high-resolution anatomical images (e.g., Figures 2A–2C, Figures 5A and 5B, and Figures 6A and 6B), which were also quite reproducible. These images, termed high-resolution sagittal scout images, were important for precisely prescribing other slices at the same locations over different sessions.

To determine the V1/V2 borders on the medial surface, five to six oblique slices (slice thickness = 5 mm) perpendicular to the CS were prescribed on the high-resolution sagittal scout images (e.g., slices indicated by dashed green lines in Figures 2A–2C, Figures 5A and 5B, and Figures 6A and 6B). Functional images were acquired using the 3 inch surface coil and the same EPI pulse sequence with parameters identical to those in the main ODC experiment (see below) except longer TR (TR = 500 and 600 ms for five and six slices, respectively). For subject 2, the V1/V2 borders were mapped with a 5 inch quadrature surface coil and an in-plane resolution of 0.94×0.94 mm^2. The stimulus was a vertically oriented bow tie-shaped black/white checkerboard with contrast reversal at 7.5 Hz on a gray background and was binocularly delivered to the subject's eyes. Functional images were acquired during two stimulation periods sandwiched in three control periods (with a gray screen), while the subject maintained fixated on a central fixation point.

The positions of slices to be used in the main ODC experiment were tentatively decided first. These slices contained sections of V1, in which ODCs were expected to be resolved in the main ODC experiment. We then performed eccentricity mapping to determine the extent of V1 that could be activated with our stimulation apparatus. The mapping method was similar to that used for determining the V1/V2 borders except that the stimuli were four checkerboard rings of different sizes (radius = 0–1.25°, 1.25–2.5°, 2.5–5°, and 5–10°) on a gray background. Four scans, each with a different checkerboard ring, were performed, and a composite eccentricity map was made. The retinotopy in V1 defined by the V1/V2 borders and eccentricity using these methods (Figures 2, 5, and 6) was as clear as that identified using the phase-encoding retinotopic mapping method (Sereno et al., 1995; DeYoe et al., 1996; Engel et al., 1997).

The positions of slices used in the main ODC experiment were finally determined by assessing the morphological quality of the sections of V1 selected as the main ROI for mapping ODCs. In relation to the orientation of human ODCs (Horton et al., 1990), several optimal ways for prescribing slices are illustrated in Figures 1C–1F. The results presented in this study were all based on images acquired using slices similar to those shown in Figure 1C.

The Main ODC Experiment

Functional and anatomical images were collected with a field of view (FOV) of 24×24 cm^2 and a 512×512 matrix, resulting in an in-plane resolution of 0.47×0.47 mm^2. Functional T_2*-weighted images were acquired using a multishot (32 interleaved and centrifugal k space segments) echo-planar imaging (EPI) gradient-recalled echo pulse sequence (TR [defined as the time of repetition between successive segments of a slice] = 300 ms; TE = 15 ms; flip angle = 40° [in the region of maximum sensitivity], sampling bandwidth = 102.4 kHz). A navigator echo was inserted at the beginning of each segment. Three interleaved slices (slice thickness = 3 mm) without gap were collected although the main region of interest was covered usually by one or two slices. In this scheme, a segment was acquired for each of the three slices sequentially within a single TR (300 ms), followed by another segment for each of the three slices, and so forth. An image volume was thus obtained every 9.6 s. The multishot EPI used here resulted in reduced effective dwell time (echo spacing) and, therefore, a less serious T_2* (measured 35 ms) blurring in the phase-encoding direction (~0.5 pixel) than that with the single-shot EPI. The T_2* blurring in the readout direction was even smaller. Taking the T_2* blurring into consideration, the true spatial resolution was 0.7×0.6 mm^2. This multishot EPI with 512 phase-encoding steps also gave rise to a satisfactory spatial SNR around V1 (>50:1 in single images). The temporal SNR showed a small reduction (~5%) compared to the spatial SNR due to physiological fluctuations (see below). T_1-weighted anatomical images at the same slice positions as functional images were acquired with the inversion recovery FLASH pulse sequence described above.

The paradigm for stimulus presentations consisted of alternating periods when monocular stimulation (a full-screen black/white checkerboard whose contrast was reversed at 7.5 Hz) was given to the left (L) or right (R) eye, separated by control dark periods (D) when black screens were presented to both eyes. In the experiment, the subject was instructed to fixate on a central fixation point during both stimulation and dark periods. When one eye was stimulated, the opposite eye was exposed to a black screen. Each monocular stimulation lasted 115.2 s and each dark period lasted 57.6 s, which

allowed the poststimulus undershoot to return back to the baseline. In total, 150 images (temporal resolution, 9.6 s) were collected for each slice over a period of ~24 min in the following sequence (each number in parentheses denotes the number of images): D(6)-L(12)-D(6)-R(12)-D(6)-L(12)-D(6)-R(12)-D(6)-L(12)-D(6)-R(12)-D(6)-L(12)-D(6)-R(12)-D(6). The steady state was achieved prior to the first dark period by exposing both eyes to the checkerboard stimulation. Thus, even the first monocular stimulation period was preceded with a dark period whose temporal characteristics (undershoot and recovery) resembled those of the remaining dark periods.

Data Processing and Analysis

Much effort was exerted to minimize signal fluctuations unrelated to the visual stimulation, including the brain pulsation (<0.5 mm in the cerebral periphery [Poncelet et al., 1992]) and rigid head motion. The EPI pulse sequence used in the present study included a navigator echo acquired at the beginning of each segment. The correction for intersegment phase and amplitude variations using this navigator echo reduced signal fluctuations due to pulsatile and rigid head motions (Hu and Kim, 1994; Kim et al., 1996). After EPI images were reconstructed, physiological (cardiac and respiratory) fluctuations were further removed from time series images using a retrospective estimation and correction method with the pulsation and respiration data recorded during image acquisition (Hu et al., 1995). In-plane rigid head motions were minimized in our experiments but were nevertheless corrected using a decoupled automated rotational and translational registration method proposed by Maas and colleagues (Maas et al., 1997). Both physiological and motion corrections were performed in the k space. In addition, a zero-frequency notch filter was used to remove the linear trend remaining in time series images, which was most likely caused by system drifts, as it was also observed in the images acquired using a phantom. Although the quality of raw data was of fundamental importance, these corrections were shown to be both necessary and effective.

As exemplified for an ODC experiment (subject 1), the maximum range and standard deviation of the in-plane center-of-mass fluctuation of time series images before the corrections for physiological fluctuations, rigid head motions and system drifts were 0.59 and 0.11 pixel (corresponding to 0.28 and 0.05 mm) in the right-left direction and 0.73 and 0.15 pixel (0.34 and 0.07 mm) in the anteroposterior direction (Figure 3A). The values in the right-left direction likely reflected real motions, while a substantial amount of fluctuation in the anteroposterior direction was likely caused by the periodic activation of the visual cortex by the visual stimulation (this is evident when traces in Figure 3A are viewed upside down). The visual cortex is located in the posterior portion of the brain. In addition, tiny linear trends are also present in the two traces. After corrections, the fluctuation was reduced to 0.53 and 0.09 pixel (0.25 and 0.04 mm) in the right-left direction and 0.71 and 0.14 pixel (0.33 and 0.06 mm) in the anteroposterior direction (Figure 3B). Similar amounts of fluctuation after corrections were also measured from a second subject (subject 2) (Figure 3C). We also measured the fluctuation from a phantom with identical imaging parameters. After the system drifts were removed, the values were 0.28 and 0.05 pixel (0.13 and 0.02 mm) in the right-left direction and 0.21 and 0.04 pixel (0.10 and 0.02 mm) in the anteroposterior direction (Figure 3D). Comparing the values obtained from the subjects before and after corrections with those from the phantom (with fluctuation only about 50% smaller), we conclude that motions of various sources in our experiments are minimized during the data acquisition and further corrected in the postprocessing.

All statistical analyses were performed using the software package STIMULATE developed at the University of Minnesota (J.P. Strupp, NeuroImage 3, S607, 1996). Activated voxels (displaying positive signal changes) were identified by the Student's t test (*one-tailed* [p values were converted from two-tailed p values used in STIMULATE]) comparing images acquired during stimulation periods and those acquired during control periods on a voxel-by-voxel basis.

To account for the hemodynamic delay, the first image acquired in each period was excluded. The problem contributed by large veins running on the brain surface to the BOLD signal was minimized in our study owing to the following reasons. First, it has been shown that the BOLD signal coming from large veins, compared with that originating in capillaries and vertically penetrating venules in the brain tissue (gray matter), is much smaller at 4 T than that at lower magnetic fields (for review, see Ogawa et al., 1998). Second, we removed the activated voxels that overlapped with large vessels outside the gray matter by the known fact that percentage signal changes in large vessels are much larger than those in the gray matter, especially at high magnetic fields (Menon et al., 1993; Gati et al., 1997; Luh et al., 2000). With the high spatial resolution employed in the present study, activated voxels confined to the gray matter and voxels associated with large veins could be satisfactorily separated by setting a threshold for the percentage signal change, and the latter were excluded from further analyses. A 5% signal change ($p < 0.05$) was used as the threshold, which was empirically determined after examining the time courses of activated voxels inside and outside the gray matter. In the example shown in Figures 3E–3G, the average signal change during both left and right eye stimulation relative to control dark periods was 9.92% for activated voxels in large vessels outside the gray matter (Figures 3E and 3F) and 1.91% for those in the gray matter (Figure 3G). In the gray matter, a vast majority of activated voxels (82.4%) had signal changes of less than 3%, and only a small portion of activated voxels (2.6%) had signal changes between 4.5% and 5%. Very similar values were also obtained in other experiments. Five percent, therefore, appeared to be an ideal threshold for separating the gray matter from large veins for the imaging parameters used in our experiment. It should be noted that the percentage signal change used here was relative to the average signal intensity of all the data points of each dark period except the first one. The average thus obtained was lower than the actual baseline intensity due to the poststimulation undershoot.

Images acquired in the experiments mapping the V1/V2 borders and eccentricity were spatially smoothed with a Gaussian filter (FWHM = 3.5 in-plane pixels) before statistical analyses were performed ($p < 0.005$, uncorrected). For clarity, only clusters of ten or more connected voxels were shown in the resulting maps.

For time series images acquired in the main ODC experiment, no spatial or temporal smoothing was applied after the postprocessing corrections. After large veins were removed, two types of maps were generated from these time series images. A pair of *activation maps* was first generated by identifying voxels displaying significant responses ($p < 0.05$) to left eye (L > D) or right eye (R > D) stimulation compared with dark periods, where L, R, and D denote time series images collected during left eye stimulation, right eye stimulation, and control dark periods, respectively. Only clusters consisting of at least three connected voxels were displayed in the activation maps.

An *ODC map* was then created. First, a pair of left and right eye dominant maps was generated using the differential mapping method by identifying significantly activated voxels in the L > D map that responded more to left eye stimulation than to right eye stimulation (L > D and L > R) and those in the R > D map that responded more to right eye stimulation (R > D and R > L). No clustering threshold was applied to the left and right eye dominant maps. The two maps were then combined to make the final ODC map. The significance level of the ODC map was the multiplication of the two original tests' significance levels. While the significance level for the activation maps (L > D and R > D, respectively) was kept at $p < 0.05$, we varied the significance level for direct comparisons between responses to left and right eye stimulation (L > R and R > L, respectively) from $p < 0.05$, $p < 0.15$, $p < 0.25$, $p < 0.35$ to $p < 0.5$, which resulted in five ODC maps at $p < 0.0025$, $p < 0.0075$, $p < 0.0125$, $p < 0.0175$, and $p < 0.025$. These p values (referred to as ODC maps' p values) were arbitrarily selected because the number of identified voxels in the corresponding ODC maps increased roughly linearly within this range (see Results and Figure 8G). This manipulation allowed us to assess the strength of differential responses and to examine spatial patterns formed by voxels displaying differential responses of various strengths. The baseline used for quantifying responses was estimated by averaging the last two points of each dark period (40–60 s after the cessation of stimulation), at which the signal time course had recovered from the poststimulation undershoot.

Acknowledgments

This work was partially supported by Core Research for Evolutionary Science and Technology (CREST), Japan Science and Technology Corporation (JST), Japan. We would like to express our gratitude to Tameng Ong, Hiroshige Takeichi, Kenichi Ueno, and Eiji Yoshitome for their assistance, to Ravi Menon for providing us with the EPI pulse sequence and image reconstruction program, to Jonathan Horton for giving us figures showing human ODCs, and to Roger Tootell for advice on the bite-bar system.

Received July 3, 2001; revised October 3, 2001.

References

Blasdel, G.G. (1992). Differential imaging of ocular dominance and orientation selectivity in monkey striate cortex. J. Neurosci. *12*, 3115–3138.

Blasdel, G.G., and Salama, G. (1986). Voltage-sensitive dyes reveal a modular organization in monkey striate cortex. Nature *321*, 579–585.

Buxton, R.B., and Frank, L.R. (1997). A model for the coupling between cerebral blood flow and oxygen metabolism during neural stimulation. J. Cereb. Blood Flow Metab. *17*, 64–72.

Callaway, E.M. (1998). Local circuits in primary visual cortex of the macaque monkey. Annu. Rev. Neurosci. *21*, 47–74.

Davis, T.L., Kwong, K.K., Weisskoff, R.M., and Rosen, B.R. (1998). Calibrated functional MRI: mapping the dynamics of oxidative metabolism. Proc. Natl. Acad. Sci. USA *95*, 1834–1839.

Dechent, P., and Frahm, J. (2000). Direct mapping of ocular dominance columns in human primary visual cortex. NeuroReport *11*, 3247–3249.

DeYoe, E.A., Carman, G.J., Bandettini, P., Glickman, S., Wieser, J., Cox, R., Miller, D., and Neitz, J. (1996). Mapping striate and extrastriate visual areas in human cerebral cortex. Proc. Natl. Acad. Sci. USA *93*, 2382–2386.

Duvernoy, H.M., Delon, S., and Vannson, J.L. (1981). Cortical blood vessels of the human brain. Brain Res. Bull. *7*, 519–579.

Engel, S.A., Glover, G.H., and Wandell, B.A. (1997). Retinotopic organization in human visual cortex and the spatial precision of functional MRI. Cereb. Cortex *7*, 181–192.

Ernst, T., and Hennig, I. (1994). Observation of a fast response in functional MR. Magn. Reson. Med. *32*, 146–149.

Florence, S.L., and Kaas, J.H. (1992). Ocular dominance columns in area 17 of old world macaque and talapoin monkeys: complete reconstructions and quantitative analyses. Vis. Neurosci. *8*, 449–462.

Fransson, P., Kruger, G., Merboldt, K.-D., and Frahm, J. (1998). Temporal characteristics of oxygenation-sensitive MRI responses to visual activation in humans. Magn. Reson. Med. *39*, 912–919.

Gati, J.S., Menon, R.S., Ugurbil, K., and Rutt, B.K. (1997). Experimental determination of the BOLD field strength dependence in vessels and tissue. Magn. Reson. Med. *38*, 296–302.

Grinvald, A., Slovin, H., and Vanzetta, I. (2000). Non-invasive visualization of cortical columns by fMRI. Nat. Neurosci. *3*, 105–107.

Hitchcock, P.F., and Hickey, T.L. (1980). Ocular dominance columns: evidence for their presence in humans. Brain Res. *182*, 176–179.

Hoge, R.D., Atkinson, J., Gill, B., Crelier, G.R., Marrett, S., and Pike, G.B. (1999). Linear coupling between cerebral blood flow and oxygen consumption in activated human cortex. Proc. Natl. Acad. Sci. USA *96*, 9403–9408.

Horton, J.C. (1984). Cytochrome oxidase patches: a new cytoarchitectonic feature of monkey visual cortex. Philos. Trans. R. Soc. Lond. Biol. B *304*, 199–253.

Horton, J.C., and Hedley-Whyte, E.T. (1984). Mapping of cytochrome oxidase patches and ocular dominance columns in human visual cortex. Philos. Trans. R. Soc. Lond. Biol. B *304*, 255–272.

Horton, J.C., and Hocking, D.R. (1998). Monocular core zones and binocular border strips in primate striate cortex revealed by the contrasting effects of enucleation, eyelid suture, and retinal laser lesions on cytochrome oxidase activity. J. Neurosci. *18*, 5433–5455.

Horton, J.C., and Hoyt, W.F. (1991). The representation of the visual field in human striate cortex. Arch. Ophthalmol. *109*, 816–824.

Horton, J.C., Dagi, L.R., McCrane, E.P., and de Monasterio, F.M. (1990). Arrangement of ocular dominance columns in human visual cortex. Arch. Ophthalmol. *108*, 1025–1031.

Hu, X., and Kim, S.-G. (1994). Reduction of signal fluctuation in functional MRI using navigator echoes. Magn. Reson. Med. *31*, 495–503.

Hu, X., Le, T.H., Parrish, T., and Erhard, P. (1995). Retrospective estimation and correction of physiological fluctuation in functional MRI. Magn. Reson. Med. *34*, 201–212.

Hu, X., Le, T.H., and Ugurbil, K. (1997). Evaluation of the early response in fMRI in individual subjects using short stimulus duration. Magn. Reson. Med. *37*, 877–884.

Hubel, D.H., and Wiesel, T.N. (1962). Receptive field, binocular interaction and functional architecture in the cat's visual cortex. J. Physiol. *160*, 106–154.

Hubel, D.H., and Wiesel, T.N. (1968). Receptive fields and functional architecture of monkey striate cortex. J. Physiol. Lond. *195*, 215–243.

Hubel, D.H., and Wiesel, T.N. (1972). Laminar and columnar distribution of geniculo-cortical fibers in macaque monkeys. J. Comp. Neurol. *146*, 421–450.

Jones, M., Berwick, J., Johnston, D., and Mayhew, J. (2001). Concurrent optical imaging spectroscopy and laser-doppler flowmetry: the relationship between blood flow, oxygenation, and volume in rodent barrel cortex. NeuroImage *13*, 1002–1015.

Kennedy, C., Des Rosiers, M.H., Sakurada, O., Shinohara, M., Reivich, M., Jehle, J.W., and Sokoloff, L. (1976). Metabolic mapping of the primary visual system of the monkey by means of the autoradiographic [14C] deoxyglucose technique. Proc. Natl. Acad. Sci. USA *73*, 4230–4234.

Kim, S.-G., Hu, X., Adriany, G., and Ugurbil, K. (1996). Fast interleaved echo-planar imaging with navigator: high resolution anatomic and functional images at 4 Tesla. Magn. Reson. Med. *35*, 895–902.

Kim, S.-G., Rostrup, E., Larsson, H.B.W., Ogawa, S., and Paulson, O.B. (1999). Determination of relative CMRO2 from CBF and BOLD changes: significant increase of oxygen consumption rate during visual stimulation. Magn. Reson. Med. *41*, 1152–1161.

Kim, D.-S., Duong, T.Q., and Kim, S.-G. (2000). High-resolution mapping of iso-orientation columns by fMRI. Nat. Neurosci. *3*, 164–169.

Leuba, G., and Kraftsik, R. (1994). Changes in volume, surface estimate, three-dimensional shape and total number of neurons of the human primary visual cortex from midgestation until old age. Anat. Embryol. *190*, 351–366.

Lindauer, U., Royl, G., Leithner, C., Kuhl, M., Gold, L., Gethmann, J., Kohl-Bareis, M., Villringer, A., and Dirnagl, U. (2001). No evidence for early decrease in blood oxygenation in rat whisker cortex in response to functional activation. NeuroImage *13*, 986–999.

Luh, W.-M., Wong, E.C., Bandettini, P.A., Ward, B.D., and Hyde, J.S. (2000). Comparison of simultaneously measured perfusion and BOLD signal increases during brain activation with T_1-based tissue identification. Magn. Reson. Med. *44*, 137–143.

Maas, L.C., Frederick, B. deB., and Renshaw, P.F. (1997). Decoupled automated rotational and translational registration for functional MRI time series data: the DART registration algorithm. Magn. Reson. Med. *37*, 131–139.

Malach, R., Amir, Y., Harel, M., and Grinvald, A. (1993). Relationship between intrinsic connections and functional architecture revealed by optical imaging and in vivo targeted biocytin injections in primate striate cortex. Proc. Natl. Acad. Sci. USA *90*, 10469–10473.

Malonek, D., and Grinvald, A. (1996). Interactions between electrical activity and cortical microcirculation revealed by imaging spectroscopy: implications for functional brain mapping. Science *272*, 551–554.

Malonek, D., Dirnagl, U., Lindauer, U., Yamada, K., Kanno, I., and Grinvald, A. (1997). Vascular imprints of neuronal activity: relationships between the dynamics of cortical blood flow, oxygenation,

and volume changes following sensory stimulation. Proc. Natl. Acad. Sci. USA *94*, 14826–14831.

Menon, R.S., and Goodyear, B.G. (1999). Submillimeter functional localization in human striate cortex using BOLD contrast at 4 Tesla: implications for the vascular point-spread function. Magn. Reson. Med. *41*, 230–235.

Menon, R.S., Ogawa, S., Tank, D.W., and Ugurbil, K. (1993). 4 Tesla gradient recalled echo characteristics of photic stimulation-induced signal changes in the human primary visual cortex. Magn. Reson. Med. *30*, 380–386.

Menon, R.S., Ogawa, S., Hu, X., Strupp, J.P., Anderseon, P., and Ugurbil, K. (1995). BOLD based functional MRI at 4 Tesla includes a capillary bed contribution: echo-planar imaging correlates with previous optical imaging using intrinsic signals. Magn. Reson. Med. *33*, 453–459.

Menon, R.S., Ogawa, S., Strupp, J.P., and Ugurbil, K. (1997). Ocular dominance in human V1 demonstrated by functional magnetic resonance imaging. J. Neurophysiol. *77*, 2780–2787.

Ogawa, S., Lee, T.-M., Kay, A.R., and Tank, D.W. (1990). Brain magnetic resonance imaging with contrast dependent on blood oxygenation. Proc. Natl. Acad. Sci. USA *87*, 9868–9872.

Ogawa, S., Menon, R.S., Kim, S.-G., and Ugurbil, K. (1998). On the characteristics of functional magnetic resonance imaging of the brain. Annu. Rev. Biophys. Biomol. Struc. *27*, 447–474.

Ono, M., Kubik, S., and Abernathey, C.D. (1990). Atlas of the cerebral sulci. (New York, NY: Thieme).

Poncelet, B.P., Wedeen, V.J., Weisskoff, R.M., and Cohen, M.S. (1992). Brain parenchyma motion: measurement with cine echo-planar MR imaging. Radiol. *185*, 645–651.

Schwarzbauer, C., and Heinke, W. (1999). Investigating the dependence of BOLD contrast on oxidative metabolism. Magn. Reson. Med. *41*, 537–543.

Sereno, M.I., Dale, A.M., Reppas, J.B., Kwong, K.K., Belliveau, J.W., Brady, T.J., Rosen, B.R., and Tootell, R.B.H. (1995). Borders of multiple visual areas in humans revealed by functional magnetic resonance imaging. Science *268*, 889–893.

Tootell, R.B., Hamilton, S.L., Silverman, M.S., and Switkes, E. (1988). Functional anatomy of macaque striate cortex. I. Ocular dominance, binocular interactions, and baseline conditions. J. Neurosci. *8*, 1500–1530.

Ts'o, D.Y., Frostig, R.D. Lieke, E.E., and Grinvald, A. (1990). Functional organization of primate visual cortex revealed by high resolution optical imaging. Science *249*, 417–420.

Turner, R., Le Bihan, D., Moonen, C.T.W., DesPres, D., and Frank, J. (1991). Echo-planar time course MRI of cat brain oxygenation changes. Magn. Reson. Med. *22*, 159–166.

Turner, R., Jezzard, P., Wen, H., Kwong, K.K., Le Bihan, D., Zeffiro, T., and Balaban, R.S. (1993). Functional mapping of the human visual cortex at 4 and 1.5 Tesla using deoxygenation contrast EPI. Magn. Reson. Med. *29*, 277–279.

Wiesel, T.N., Hubel, D.H., and Lam, D.M.K. (1974). Autoradiographic demonstration of ocular dominance columns in the monkey striate cortex by means of transneuronal transport. Brain Res. *79*, 273–279.

Wiser, A.K., and Callaway, E.M. (1997). Ocular dominance columns and local projections of layer 6 pyramidal neurons in macaque primary visual cortex. Vis. Neurosci. *14*, 241–251.

Yacoub, E., and Hu, X. (1999). Detection of the early negative response in fMRI at 1.5 Tesla. Magn. Reson. Med. *41*, 1088–1092.

Yacoub, E., Shmuel, A., Pfeuffer, J., Van De Moortele, P.-F., Adriany, G., Andersen, P., Vaughan, J.T., Merkel, H., Ugurbil, K., and Hu, X. (2001). Imaging brain function in humans at 7 Tesla. Magn. Reson. Med. *45*, 588–594.

Yoshioka, T., Blasdel, G.G., Levitt, J.B., and Lund, J.S. (1996). Relation between patterns of intrinsic lateral connectivity, ocular dominance, and cytochrome oxidase-reactive regions in macaque monkey striate cortex. Cereb. Cortex *6*, 297–310.